



*Citation for published version:*

Glavini, I, Muttakin, I, Abouelazayem, S, Blishchik, A, Stefani, F, Eckert, S, Soleimani, M, Saidani, I, Hlava, J, Kenjereš, S & Wonderak, T 2022, 'Laboratory investigation of tomography-controlled continuous steel casting', *Sensors*, vol. 22, no. 6, 2195. <https://doi.org/10.3390/s22062195>

*DOI:*

[10.3390/s22062195](https://doi.org/10.3390/s22062195)

*Publication date:*

2022

*Document Version*

Peer reviewed version

[Link to publication](#)

*Publisher Rights*

CC BY

**University of Bath**

**Alternative formats**

If you require this document in an alternative format, please contact:  
[openaccess@bath.ac.uk](mailto:openaccess@bath.ac.uk)











**General rights**

Copyright and moral rights for the publications made accessible in the public portal are retained by the authors and/or other copyright owners and it is a condition of accessing publications that users recognise and abide by the legal requirements associated with these rights.

**Take down policy**

If you believe that this document breaches copyright please contact us providing details, and we will remove access to the work immediately and investigate your claim.

# Laboratory investigation of tomography-controlled continuous steel casting

Ivan Glavinic<sup>1\*</sup> , Imamul Muttakin<sup>2</sup> , Shereen Abouelazayem<sup>3</sup> , Artem Blishchik<sup>4</sup> , Frank Stefani<sup>1</sup> , Sven Eckert<sup>1</sup> , Manuchehr Soleimani<sup>2</sup> , Iheb Saidani<sup>1</sup>, Jaroslav Hlava<sup>3</sup> , Saša Kenjereš<sup>4</sup> , and Thomas Wondrak<sup>1</sup> 

<sup>1</sup> Helmholtz-Zentrum Dresden - Rossendorf, Bautzner Landstraße 400, Dresden, Germany

<sup>2</sup> University of Bath, Claverton Down, Bath, United Kingdom

<sup>3</sup> Technical University of Liberec, Studentská 1402/2, Liberec, Czech Republic

<sup>4</sup> Delft University of Technology, van der Maasweg 9, Delft, Netherlands

\* Correspondence: i.glavinic@hzdr.de

**Abstract:** More than 96% of steel in the world is produced via the method of continuous casting. The flow condition in the mould, where the initial solidification occurs, has a significant impact on the quality of steel products. It is important to have timely, and perhaps automated, control of the flow during casting. This work presents a new concept of using Contactless Inductive Flow Tomography (CIFT) as a sensor for a novel controller, which alters the strength of an Electromagnetic Brake (EMBr) of ruler type based on the reconstructed flow structure in the mould. The method was developed for the liquid metal model mini-LIMMCAST available at the Helmholtz-Zentrum Dresden - Rossendorf. As an example of an undesired flow condition, clogging of the Submerged Entry Nozzle (SEN) was modelled by partly closing one of the side ports of the SEN, in combination with an active EMBr the jet penetrates deeper into the mould than when the EMBr is switched off. Corresponding flow patterns are detected by extracting the impingement position of the jets at the narrow faces of the mould from the CIFT reconstruction. The controller is designed to detect to undesired flow condition and switch off the EMBr. The temporal resolution of CIFT is 0.5 second.

**Keywords:** Contactless Inductive Flow Tomography; Continuous casting; Clogging; Flow control, EMBr, Inductive measurements, mini-LIMMCAST

## 1. Introduction

When it comes to controlling industrial processes, it is paramount to have reliable and accurate measurements and a detailed understanding of the underlying process. However, in the case of continuous casting of steel, due to the aggressive environment, measuring any variable of interest is challenging. In this process, liquid steel is brought by ladles and poured in the tundish, which acts as a buffer storage between ladle changes. From the tundish, steel flows through the Submerged Entry Nozzle (SEN) into the water-cooled mould where the initial solid shell is formed. A solid shell with a liquid core is continuously extruded from the underside of the mould and further cooled and guided to the subsequent processes. Conditions during casting and the flow pattern in the mould are relevant for the quality of the end products [1,2]. In order to influence the flow in the mould, different electromagnetic actuators were developed in the last decades, which do not require any direct contact to the melt. Typical systems are electromagnetic stirrers and electromagnetic brakes (EMBr) [4]. Systems with different magnetic field shapes for slab casters are available: the ruler and double-ruler EMBr, local braking, electromagnetic stirring at the meniscus and/or at the strand, and a combination of a stirrer at the meniscus level and an EMBr of ruler-type below the SEN. The control of these actuators based on the current flow structure in the mould would be desirable.

However, opaqueness and high temperatures of the liquid steel make it nearly impossible to use conventional flow measurement methods. The nail-bed dipping

**Citation:** . *Sensors* **2021**, *11*, 0.  
<https://doi.org/>

Received:

Accepted:

Published:

**Publisher's Note:** MDPI stays neutral with regard to jurisdictional claims in published maps and institutional affiliations.

**Copyright:** © 2022 by the authors. Submitted to *Sensors* for possible open access publication under the terms and conditions of the Creative Commons Attribution (CC BY) license (<https://creativecommons.org/licenses/by/4.0/>).

37 technique is widely used to get a coarse instantaneous subsurface velocity profile [5],  
38 and measurements of the inclination of an immersed paddle yield continuous but  
39 localized information of the velocity [7]. Both methods are difficult to be used for  
40 online monitoring. Contactless methods for local velocity measurements exploit the  
41 high electrical conductivity of the liquid steel and rely on the principle of induction.  
42 Recently, Lorentz Force Velocimetry was tested to monitor the meniscus velocity in a  
43 steel caster [8]. The downside of localized velocity measurements is that information is  
44 provided only at a single point or small region in space, while several sensors would  
45 be needed to capture the overall flow pattern. There is a need for multidimensional  
46 measurements that can provide information-rich data for measurement during casting.  
47 Recently, a new measurement technique for temperature distribution in the copper walls  
48 of the mould using Fiber-Bragg gratings [9,10] became available. This technique allows  
49 to detect the spatially resolved shape of the meniscus in real time. From the shape  
50 of the meniscus some general assumptions of the flow structure in the mould can be  
51 made. A different approach is the measurement of the local velocity and the use of  
52 numerical simulations to infer the velocity structure in the mould. Zhang et al. use  
53 an immersed paddle to measure the sub-meniscus flow velocity in connection with a  
54 complex mathematical model that combines computational fluid dynamics and discrete  
55 phase method [11]. Hashimoto et al. developed a real-time flow estimation algorithm  
56 based on three-dimensional transient modelling in order to obtain information on the  
57 steel flow. However, this approach was validated by simulations only [12].

58 In the absence of direct measurements of the flow field, the EMBr are usually  
59 controlled by process parameters or by product recipes. Due to the limited data from  
60 the real process, the operation parameters are identified using process modelling tech-  
61 niques, either numerical or physical, which in turn enables the development of new  
62 strategies and measurement methods. Numerical methods can provide deep knowledge  
63 of physical processes and phenomena, but they require a lot of computational resources  
64 for just a single scenario [13,14]. Thus, it is complicated to use them in order to test new  
65 control methodologies. Furthermore, they need to be validated using experimental data  
66 provided by the physical models. By contrast, physical models also enable much larger  
67 parameter studies [15]. Specifically, for continuous casting, we can distinguish between  
68 two types of physical models: water models [16] and liquid metal models [17,18]. Both  
69 types have their advantages and disadvantages. Water models are easier to operate  
70 and built on a 1:1 scale, and optical methods can be employed for flow measurement.  
71 However, since water is electrically non-conductive, it is impossible to model the effects  
72 of the electromagnetic actuators. Liquid metal models allow for such investigation, but  
73 they are more difficult to build, maintain, and operate.

74 The development of control loops for EMBr based on real-time flow measurements  
75 just started quite recently. Dekemele et al. investigated the feasibility to develop a  
76 control loop for an electromagnetic stirrer using a travelling magnetic field in the region  
77 of the jet based on sub-meniscus flow measurements with an immersed paddle [19].  
78 Recently, a successful approach of controlling the strength of an EMBr for a thin caster  
79 by measuring the shape of the meniscus using Fiber-Bragg gratings was reported [20].  
80 Other control variables, such as stopper rod position, amount of Argon gas, and even  
81 casting speed, could, in theory, be modulated, but their master controller is part of the  
82 system ensuring safe and stable operation, i.e. position of the stopper rod is controlled  
83 by the mould level controller.

84 The use of inductive tomographic sensors for continuous casting control has not yet  
85 been studied. Lately, two different inductive measurement modalities were developed,  
86 Mutual Inductance Tomography (MIT) which can provide spatially resolved distribution  
87 of gas/liquid distribution in the SEN [21], and Contactless Inductive Flow Tomography  
88 (CIFT) which can reconstruct the flow structure of the liquid steel in the mould [22].  
89 While these techniques are not yet used in the production environment, they present

90 interesting opportunities to visualize the global three-dimensional flow in the mould  
91 and the SEN in real time.

92 MIT is able to reconstruct the conductivity distribution in one cross-section of the  
93 SEN, and thereby distinguish between liquid metal and argon gas in case of a two-  
94 phase flow in a physical model [23,24]. Tomographic data/images as well as SEN filling  
95 profiles would be useful data for the control implementation. However, the challenges  
96 remain for dynamic liquid metal two-phase flow measurements. Small distributed inner  
97 bubbles are difficult to detect and reconstruct. The multi-frequency method, bypassing  
98 reconstruction and using just raw data, or data driven approaches for quantification are  
99 the future directions that could be investigated for continuous casting [25].

100 CIFT relies on measuring the perturbations of an applied magnetic field (primary  
101 field) caused by the movement of the conductive fluid [22,26]. The potential of CIFT to  
102 reconstruct the velocity structure has been demonstrated in the laboratory model of a  
103 continuous caster [27], as well as in other laboratory experiments that model Rayleigh-  
104 Benard convection and Czochralski crystal growth [28]. The main advantage of CIFT, in  
105 comparison to other measurement techniques, is that the measurements of the magnetic  
106 field are done outside the fluid, and it is able to reconstruct the essential structures  
107 of the global flow field. However, the challenge is detecting the small flow-induced  
108 perturbation of the applied magnetic field which is in the order of several hundred nT,  
109 in particular as it is very sensitive to ferromagnetic parts close to the sensor and the  
110 environmental magnetic field, e.g. generated by currents in cables. This sensitivity can  
111 be reduced by developing specialized and highly sensitive coils that measure the spatial  
112 gradient of the magnetic field, almost eliminating the influence of magnetic fields which  
113 are uniform along the sensor axis [29,30], i.e. Earth's magnetic field. It has been shown  
114 that CIFT can reconstruct the velocity in the presence of a static magnetic field of the  
115 EMBr [31,32], and even if the EMBr strength is changed during the measurement [33]. A  
116 real-time reconstruction algorithm has been proposed enabling a real-time monitoring  
117 of the flow [34].

118 In this paper we demonstrate, for the first time, an automatic control of a ruler  
119 EMBr based on the CIFT reconstruction of the flow in the mould of the mini-LIMMCAST  
120 facility at the Helmholtz-Zentrum Dresden - Rossendorf. The model is operated with  
121 a eutectic alloy GaInSn, which is liquid at room temperature. The mould has a cross-  
122 section of  $300 \times 35 \text{ mm}^2$  [15,18]. The model is used for the study of flow phenomena in  
123 the mould and is operated in isothermal mode. Recently, a systematic parameter study  
124 was conducted to investigate the influence of the position of the EMBr on the flow using  
125 Ultrasound Doppler Velocimetry (UDV) [15]. Based on these UDV measurements, we  
126 investigated the possibility to develop control loops for mini-LIMMCAST [35].

127 In order to show the feasibility of a control loop based on CIFT measurements, we  
128 equipped the mould of mini-LIMMCAST with a CIFT sensor which can compensate  
129 for the changes of the EMBr strength, and developed a clogging model, which is used  
130 to introduce a disturbance in the form of the flow asymmetry. It turned out that this  
131 asymmetry is enhanced when the EMBr is active. Therefore, we decided to develop a  
132 disturbance rejection controller, which detects the actual impingement position of the jet  
133 at both narrow faces of the mould and turns off the EMBr if the difference between the  
134 impingement positions is above a critical threshold for a given time.

135 After a short description of the laboratory model and the operating principles  
136 of CIFT, we will explain the compensation of the effects of the EMBr on the CIFT  
137 measurement and the influence of the clogging model on the flow in the mould. Then,  
138 we describe the design of the controller and the results of the automatic control. Finally,  
139 we give an outlook of proposed future work.

## 140 2. Experimental setup

### 141 2.1. Contactless Inductive Flow Tomography

142 Contactless Inductive Flow Tomography is a method for reconstructing the three-  
143 dimensional velocity structure of a conductive fluid by measuring the perturbations of an  
144 applied magnetic field caused by the flow structure. Consider the fluid with conductivity  
145  $\sigma$  flowing in a magnetic field  $\mathbf{B}$ , according to the Ohm's law, an eddy current will be  
146 induced:

$$\mathbf{j} = \sigma(\mathbf{B} \times \mathbf{v} - \nabla\varphi), \quad (1)$$

147 where  $\varphi$  is the potential along the fluid boundaries. The current  $\mathbf{j}$  gives rise to the  
148 secondary magnetic field according to Biot-Savarts law:

$$\mathbf{b}(\mathbf{r}) = \frac{\mu_0}{4\pi} \iiint_V \mathbf{j} \times \frac{\mathbf{r} - \mathbf{r}'}{|\mathbf{r} - \mathbf{r}'|^3} dV, \quad (2)$$

149 where  $V$  is the fluid domain,  $\mathbf{r}$  is a position in space outside the fluid domain and  $\mathbf{r}'$   
150 is a position within the fluid domain.

151 The divergence free condition for the current density

$$\nabla \cdot \mathbf{j} = 0 \quad (3)$$

152 must be satisfied. By applying divergence free condition of the current to the  
153 equation (1) a Poisson equation for the electric potential arises:

$$\nabla^2 \varphi = \nabla(\mathbf{v} \times \mathbf{B}). \quad (4)$$

154 Next, by inserting equation (1) into equation (2) and resolving the Poisson equation  
155 for the electric potential, the following system of equations is obtained:

$$\mathbf{b}(\mathbf{r}) = \frac{\mu_0 \sigma}{4\pi} \iiint_V \frac{(\mathbf{v}(\mathbf{r}') \times \mathbf{B}(\mathbf{r}')) \times (\mathbf{r} - \mathbf{r}')}{|\mathbf{r} - \mathbf{r}'|^3} dV' - \frac{\mu_0 \sigma}{4\pi} \iint_S \frac{\varphi(\mathbf{r}') \mathbf{n}(\mathbf{r}') \times (\mathbf{r} - \mathbf{r}')}{|\mathbf{r} - \mathbf{r}'|^3} dS', \quad (5)$$

$$\varphi(\mathbf{r}) = \frac{1}{4\pi p(\mathbf{r})} \iiint_V \frac{(\mathbf{v}(\mathbf{r}') \times \mathbf{B}(\mathbf{r}')) \cdot (\mathbf{r} - \mathbf{r}')}{|\mathbf{r} - \mathbf{r}'|^3} dV' - \frac{1}{4\pi p(\mathbf{r})} \iint_S \frac{\varphi(\mathbf{r}') \mathbf{n}(\mathbf{r}') \cdot (\mathbf{r} - \mathbf{r}')}{|\mathbf{r} - \mathbf{r}'|^3} dS', \quad (6)$$

156 where  $p(\mathbf{r})$  is a factor between  $0 \leq p(\mathbf{r}) \leq 1$  which is determined by the shape of  
157 the boundary and depends on the solid angle of the surface at the position  $\mathbf{r}$ .  $dS'$  and  
158  $dV'$  are surface and volume elements, respectively. In principle,  $\mathbf{B}(\mathbf{r})$  is the sum of the  
159 applied (excitation) magnetic field  $\mathbf{B}_0(\mathbf{r})$  and the flow induced magnetic field  $\mathbf{b}(\mathbf{r})$ . Note,  
160 however, that the ratio of  $\mathbf{b}(\mathbf{r})$  to  $\mathbf{B}_0(\mathbf{r})$  is governed by the magnetic Reynolds number  
161  $R_m = vl\mu_0\sigma$ . For our experiment, the characteristic velocity  $v$  is the inlet velocity of 1.4  
162 m/s and the typical length scale  $l$  is the diameter of the jet of 15 mm. The electrical  
163 conductivity  $\sigma$  of GaInSn is 3.29 MS/m resulting in  $R_m = 0.086$ , which is much smaller  
164 than 1. Therefore, the problem can be considered linear for our model and the total  $\mathbf{B}$  in  
165 equation (5) and equation (6) can be replaced by the excitation magnetic field  $\mathbf{B}_0$ .

166 The (linearized) inverse problem is resolved by discretizing the domain and apply-  
167 ing the shape functions to the individual elements. Thus, the relationship between the  
168 flow induced magnetic field and the velocity of the fluid can be written in a matrix form

$$\mathbf{b} = \mathbf{M} \tilde{\mathbf{v}}, \quad (7)$$

169 where  $\mathbf{M}$  is a system matrix as derived in [26].

170 To resolve the linear inverse problem and to reconstruct the velocity field, the  
171 following expression must be minimized:

$$\min_{\tilde{\mathbf{v}}} (\|\mathbf{M} \tilde{\mathbf{v}} - \tilde{\mathbf{b}}\|_2^2 + \|\mathbf{E} \tilde{\mathbf{v}} - \mathbf{v}_{\text{inlet}}\|_2^2 + \|\mathbf{G} \tilde{\mathbf{v}}\|_2^2 + \lambda \|\mathbf{D} \tilde{\mathbf{v}}\|_2^2) \quad (8)$$

172 In this functional, the matrix  $\mathbf{E}$  is a selection matrix for the nodes of the inlet  
 173 boundary and  $\mathbf{v}_{\text{inlet}}$  is the velocity at these nodes.  $\mathbf{G}$  is a matrix that calculates the  
 174 divergence of the velocity field. The regularization parameter  $\lambda$ , which allows finding  
 175 a good compromise between minimization of the residuum and the kinetic energy of  
 176 the flow field, is selected via the L-curve method. Real-time reconstruction is done  
 177 by precomputing the inverse of the linear equation system resulting from equation (  
 178 8) for the predefined regularization parameter [34] and multiplying it with the vector  
 179 containing the flow-induced magnetic field measurements during the experiment.

180 The size of the matrices is determined by the domain discretization and is limited by  
 181 the computer memory. However, it only mildly affects the accuracy of the reconstruction  
 182 which is mostly determined by the number of available sensors. Still, even with an  
 183 infinitely dense sensor coverage of the surface the intrinsic non-uniqueness of the inverse  
 184 problem, which basically concerns the depth dependence of the velocity distribution  
 185 [22], can only be mitigated by regularization. Thus, the spatial resolution for quantifying  
 186 the quality cannot be easily defined since reconstruction quality only partially depends  
 187 on the grid size. Previous work shows that the structure of the dominating flow field  
 188 is reconstructed with a reasonable quality [27]. Here, the flow-induced magnetic field  
 189 was calculated from the numerically determined velocity field and fed to the inverse  
 190 problem solver for CIFT. The reconstructed velocity field was then compared with the  
 191 original velocity field. The mean correlation and the mean error was about 75% and 30%  
 192 for a sensor arrangement of 8 sensors along each narrow faces of the mould (Figure 8 in  
 193 [27]).

## 194 2.2. mini-LIMMCAST

195 Experiments were performed at the mini-LIMMCAST facility at Helmholtz-Zentrum  
 196 Dresden-Rossendorf. Mini-LIMMCAST is a 1:5 scaled isothermal model of a continuous  
 197 caster and is shown in Figure 1. It is operated with the eutectic alloy of Gallium-Indium-  
 198 Tin (GaInSn), which is liquid at room temperature. The liquid metal is stored in the  
 199 catchment tank, from where it is pumped to the tundish using an electromagnetic pump.  
 200 The level of the liquid metal in the tundish is continuously kept constant by controlling  
 201 the speed of the pump. From tundish, the metal flows through the SEN into the mould,  
 202 and the flow rate is controlled by the position of the stopper rod. The mould is made out  
 203 of acrylic glass and has a rectangular profile of  $300 \times 35 \text{ mm}^2$  with a height of  $620 \text{ mm}$ .  
 204 The SEN has an inner diameter of  $12 \text{ mm}$ , an outer diameter of  $21 \text{ mm}$  and two side ports  
 205 directed downward at an angle of  $15^\circ$ . The high electrical conductivity of GaInSn is  
 206 comparable to the one of liquid steel and enables the use of electromagnetic actuators  
 207 to alter the flow structure in the mould. Figure 1 shows the sketch of the experimental  
 208 setup with relative positions of SEN, mould, EMBr of ruler-type, and CIFT measurement  
 209 and excitation coils.

210 The EMBr influences the flow by generating a strong magnetic field which induces  
 211 eddy currents in a flowing metal. Because of the mutual interaction of the magnetic field  
 212 of the EMBr and the induced currents, the liquid metal will experience Lorentz forces  
 213 opposite to the direction of the fluid flow, essentially braking the fluid and altering the  
 214 flow pattern. EMBr is powered by a maximum current of 600 A, generating a magnetic  
 215 flux density up to 404 mT.

216 Measurements of the velocity at the laboratory setup can be performed either with  
 217 CIFT or UDV. While UDV provides linear profiles of the velocity component in the  
 218 direction of the ultrasound beam, it is a reliable and well-established measurement  
 219 method for liquid metals. By arranging multiple ultrasound transducers in an array,  
 220 a scalar field can be constructed containing just one velocity component. CIFT can  
 221 reconstruct the full two-dimensional velocity field. For this purpose, two excitation coils  
 222 are installed, one above and one below the ferromagnetic yoke of the EMBr. To measure



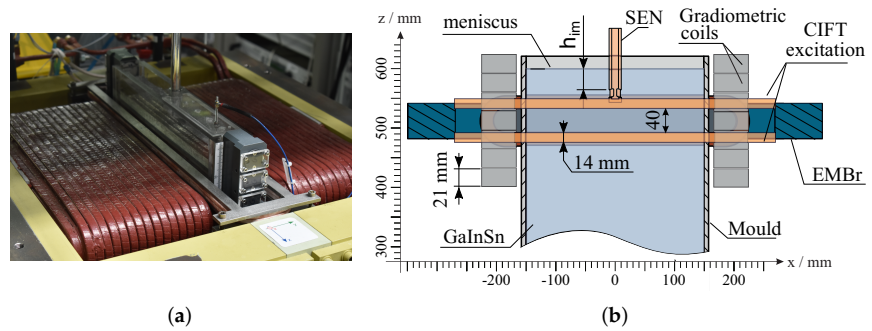


**Figure 1.** Experimental setup containing CIFT coils and sensors and the EMBr. Two excitation coils generate a primarily vertical magnetic field. Fourteen gradiometric coils, seven on each narrow side, are used to measure the flow-induced magnetic field. EMBr generates a strong magnetic field below the SEN, perpendicular to the wide side of the mould. (a) Photograph of the mould and CIFT coils. (b) Sketch adopted from Schurmann et. al. [15]

223 the flow-induced magnetic field, fourteen gradiometric coils were placed, seven on each  
 224 narrow side of the mould. The gradiometric coils consist of two counter-wound coils  
 225 connected in series. This configuration is robust in discarding the effects of uniform  
 226 magnetic fields on the measurement, e.g. Earth's magnetic field.

227 The excitation magnetic field is generated by an alternating current with frequency  
 228 of 8 Hz. By using AC excitation magnetic field, the amplitude of the flow-induced mag-  
 229 netic field is encoded at the same frequency and in-phase to the excitation magnetic field.  
 230 The demodulation is done by applying the Lomb-Scargle algorithm on the measured  
 231 voltage [36]. The flow-induced magnetic field is calculated from the sensor transfer  
 232 function and the measured induced voltage.

233 For the sake of simplicity, only one regularisation parameter ( $\lambda$  in Eq. (8)) is  
 234 selected and used for all real-time reconstruction, because it turns out that the values  
 235 of the regularisation parameter for a variety of experiments are nearly constant. From  
 236 the reconstructed velocity field, the information of the jet impingement position is  
 237 determined by finding the area within 10 mm from the narrow wall, where the average  
 238 vertical velocity is zero  $\bar{v}_z = 0 \text{ mm/s}$ .

### 239 3. Results

#### 240 3.1. Effects of the EMBr on CIFT

241 When it comes to implementing CIFT as feedback in the control loop, several chal-  
 242 lenges arise. First, the compensation of the influence of the EMBr on the measurements  
 243 is not straightforward, as it needs to compensate for the hysteresis exhibited by the  
 244 ferromagnetic parts of the EMBr. The effect of the EMBr is shown in Figure 2. Figure 2a  
 245 shows the measured flow-induced magnetic field for an experiment where the EMBr  
 246 current was changed during the run. It can be seen that the flow-induced magnetic field  
 247 changes drastically when the current through the EMBr is varied from 0 A to 200 A at  
 248  $t \approx 290 \text{ s}$ . This phenomenon can be explained by the ferromagnetic properties of the  
 249 yoke, which depend on the magnetic field generated by the coils of the brake. Therefore,  
 250 the shape of the excitation magnetic field, which is partly closing through the yoke,  
 251 also changes. This alteration is visible as a static offset of the flow-induced magnetic  
 252 field. Figure 2b shows the flow induced magnetic field after the compensation procedure  
 253 described in the following.

254 One of the properties of the magnetic hysteresis is the congruency property. This  
 255 property states that all minor hysteresis loops corresponding to the same extreme input  
 256 values are congruent in the geometrical sense [37]. So it can be expected that for two  
 257 consecutive experiments, for the same change of the EMBr current, the change of the  
 258 measurement of the flow-induced magnetic field would also be the same. Utilizing this

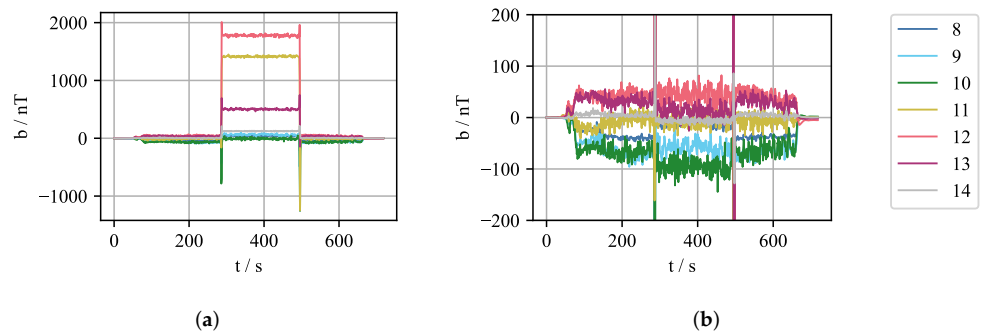


**Figure 2.** Measurement of flow-induced magnetic field during the experiment when the EMBr current changed. (a) Uncompensated flow-induced magnetic field, during the experiment the EMBr current changed from 0 A to 200 A at  $t \approx 290$  s and back to 0 A at  $t \approx 500$  s. (b) Compensated flow-induced magnetic field.

property is easy, but it is required to perform identification measurements before the measurements with fluid flow can be started.

Complex control strategies often require the actuator to assume any state, limited only by the minimum and maximum values. However, during the transitions from one set-point to another, comparably high voltages are induced in the measurement coils, and information about the flow-induced magnetic field is lost. Thus, we limit the set-point values for the  $I_{EMBr}$  to discrete levels with steps of 25 A,  $\Delta I_{EMBr} = 25A$ . Another point to consider when deciding on the congruence-based compensation is that it can only be used reliably for identified values and the transition stages. To cover the entire operation span of the EMBr current, identification should be done by cycling the EMBr current from minimum to maximum, and back to minimum. Subsequently, only the same current values, and transitions can be used for control. Consider the initial state when EMBr is switched off, and the controller sets the first set-point of the EMBr current higher than zero. If the second set-point is larger than the first one, the EMBr current must first increase to the maximum and then decrease to its new set-point. This mode of operation could introduce some undesirable effects on the flow, and it is not well-suited for complex control strategies.

A more flexible compensation method is by implementing the numerical model of the hysteresis. For this purpose, the Krasnosel'skii-Pokrovski (KP) [38] model of hysteresis was implemented that performs the compensation in real-time. However, due to the lack of precise EMBr current source and measurement method, the error introduced from the compensation, in some cases, is larger than, or in the same range of the expected flow-induced magnetic field. Figure 3 shows the compensation when using a hysteresis model for a given identification and measurement current steps. During identification, the corresponding mean value of the flow-induced magnetic field was recorded for all sensors for every current step. The measurements were used to identify the weights of the KP model using a discrete model and Least-squares method adopted from Stakvik et. al. [39]. With the determined weights of the system, the prediction of compensation can be calculated from a given set of input currents. However, even though the absolute error for the sensor shown is in order of 20 nT, the expected value of the flow-induced magnetic field is in the same order of magnitude. The underlying uncertainty makes it difficult to reconstruct the velocity field reliably, and even though the model can be improved, for the first tests of the real-time control a congruency-based compensation was used for just one value of the EMBr current, limiting the control strategy to an on/off controller. The implemented numerical KP hysteresis model inherently supports this operating mode, and with further improvements, it can be used for more complex controllers.



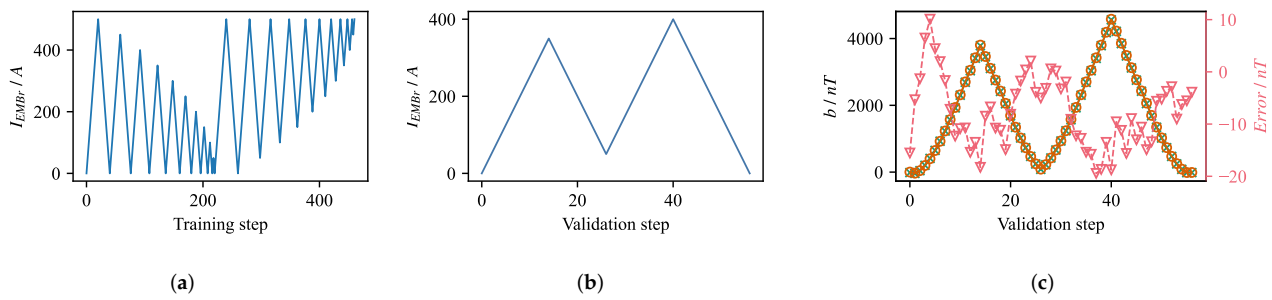


**Figure 3.** Compensation error of the KP hysteresis model. (a) Current profile used for identification of the model weights; every measurement step represents a period of fifteen seconds, during which the mean value of the flow-induced magnetic was recorded for each sensor as an input to the hysteresis model. Current is changed in steps of  $\Delta I_{EMBr} = 25$  A. (b). Current profile used to validate the accuracy of the model. For each step the corresponding value of the flow induced magnetic field is recorded and compared to the output of the model in case of the use of same current profile as an input to the model. (c) Absolute error of the model shown for the middle gradiometric coil on the right side of the mould (Sensor 4).

### 296 3.2. Control strategy

297 Previously developed control strategies that are based on UDV measurements  
 298 [35] could not be directly transferred to CIFT-based control because of the different  
 299 spatial and temporal resolution of both measurement modalities. UDV provides a finer  
 300 temporal and spatial resolution along the measurement line, and it is not influenced  
 301 by the changes of the magnetic field strength of the EMBr. But the measurements were  
 302 only conducted on one side of the mould. On the other hand, CIFT can provide a  
 303 two-dimensional velocity field for the entire fluid domain, albeit with relatively sparse  
 304 resolution which is basically related to the limited number of magnetic field sensors  
 305 and the intrinsic non-uniqueness of CIFT. The amount of nodes at which velocities are  
 306 reconstructed is limited by memory of the computer, and for our experiments it was in  
 307 the order of 10000 nodes, and the grid spatial resolution in the upper mold area is the  
 308 range between 5 and 10 mm.

309 In this study, an obstacle was introduced into the flow to generate a disturbance in  
 310 form of an asymmetric flow that can be detected by CIFT. The drawing of the obstacle  
 311 and its position with respect to the SEN is shown in Figure 4. As in [40], the obstacle  
 312 serves to simulate the situation of SEN clogging, which can be realized by reducing the  
 313 port size resulting in lower velocities at the clogged side and increased velocity and  
 314 deeper impingement on the opposite side. The obstacle used has a bevel with a  $45^\circ$   
 315 angle to ensure the asymmetry of the jet impingement position is significant enough  
 316 for detection during the real-time reconstruction. The influence of the obstacle on the  
 317 reconstructed flow field can be seen in Figure 5. Figure 5a presents the reference flow  
 318 without inserted obstacle and without active EMBr. Figure 5b is the reconstruction of  
 319 the experiment when the current through EMBr is set to  $I_{EMBr} = 200$  A; for this range of  
 320 operation of the EMBr, there is no significant effect on the jet impingement point [15].  
 321 However, if an obstacle is placed at the SEN outlet at a certain position, the flow rate  
 322 on one side is reduced, and the jet impingement point is deeper in the mould, visible  
 323 from Figure 5c. If the EMBr is then switched on, the jet seems to impinge deeper in the  
 324 mould, enhancing the asymmetry, as shown in Figure 5d. This increased asymmetry is  
 325 the scenario which the controller is trying to identify and respond to.

326 Due to the limitations on compensating the effect of the EMBr as described in the  
 327 previous section, we constrain the operation of the EMBr to two modes of operation, on-  
 328 state with  $I_{EMBr} = 200$  A and off-state. This constraint significantly reduces the training  
 329 time, from several hours for a training sequence from Figure 3a, to a few minutes for the  
 330 simpler two state changes from 0 A to 200 A and back to 0 A. The selected scenario is  
 331 realistic since, in the industrial process of steel casting, the operating current of the EMBr  
 332 is predetermined by the product recipe and is empirically selected, either from plant

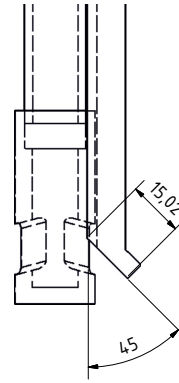


**Figure 4.** Setup of the clogging model showing the obstacle position with respect to the SEN. The obstacle is positioned to cover half of the SEN outlet and has an additional 15 mm long extension directed downward at an angle of 45°. Outlets of the SEN are directed downward at an angle of 15°

333 measurements or numerical simulations. However, in a steel caster, the SEN's clogging  
 334 generally increases over time, but for simplicity, we model it as an invariant occurrence.

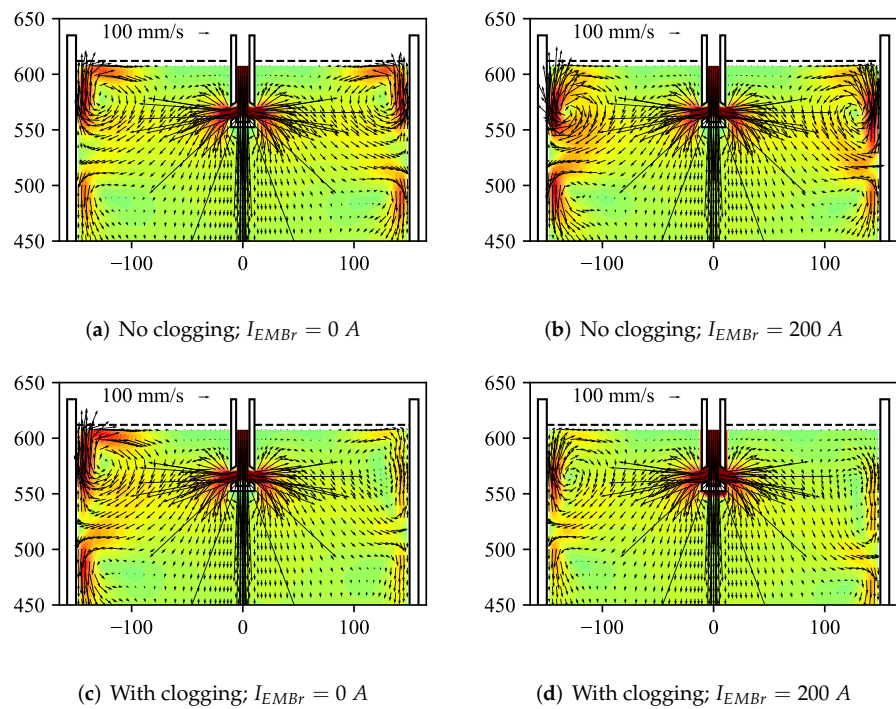


**Figure 5.** Reconstructed velocity fields in the center  $xz$ -plane of the mould for different experimental configurations.

335 The reconstructions in Figure 5 show instantaneous velocity profiles in the center  
 336 cross-section of the mould for four instants of time. The reconstructed velocity fields  
 337 are obtained by solving the minimization problem in Equation (8). Due to the turbulent  
 338 nature of the jet, the impingement position has to be time-averaged. Figure 6 shows the  
 339 time average of the jet impingement points on both narrow sides of the mould. It can be  
 340 seen that the mean jet impingement point on both sides do not differ when there is no  
 341 clogging, even when the EMBr is turned on. When clogging is introduced, a difference of  
 342 about 5 mm can be observed in the time interval between 300 and 500 s. This difference  
 343 increases significantly to 20 mm, when the EMBr current is set to  $I_{EMBr} = 200$  A. It is  
 344 clear that this condition is unwanted during casting. Based on the observed interaction

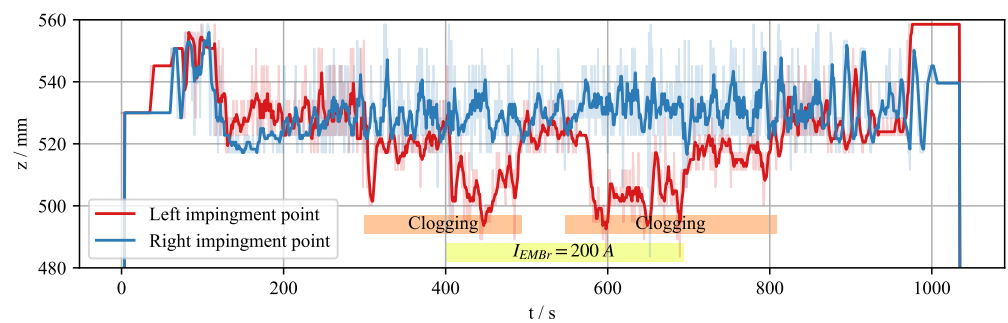


**Figure 6.** Jet impingement position at both sides of the mould. Less opaque background graph shows the raw position of the impingement point. Solid lines show the running average of the respective impingement point. Running mean window is ten samples (five seconds)

345 between EMBr, obstacle, and the flow, an on/off controller is designed which detects the  
 346 strong asymmetry in the jet impingement position, classifies it as a result of clogging  
 347 and switches off the EMBr.

348 The design of the controller can be seen in Figure 7. It receives information about  
 349 the jet impingement at both narrow faces of the mould from the real-time reconstruction  
 350 every 0.5 s. A running mean filter is then applied, and the difference between the  
 351 impingement positions of the jet on both sides is calculated. The absolute difference  
 352 between the two is an input to the *Relay operator* whose output is set to logical 1 if the  
 353 difference is larger than the value of the *Impingement Diff On* input variable, in this case,  
 354 more than 20 mm. The output is reset if the absolute difference is lower than the value  
 355 of *Impingement Diff Off* input variable. If the output from the relay operator is 1 for a set  
 356 amount of time, given by the *Time Delay*, it is evaluated with two additional conditions:  
 357 the flow must be active, set by the operator with the toggle switch, and current must  
 358 equal the desired value. The two additional conditions are necessary only for ensuring  
 359 stability and control over the experiment. If all the conditions are satisfied, a state is set  
 360 that automatically changes the current set-point to the EMBr to the desired value given  
 361 by constant *Control action*, in this case, to 0 A. A controller reset has to be performed by  
 362 the operator to avoid any toggling of the current set-point by setting the *Manual Current*  
 363 *Setpoint* to the same value of *Control action*. The current set-point is sent to the current  
 364 source for the EMBr. The complete communication diagram and block scheme of the  
 365 controller is given in the [Appendix A](#)

366 In order to prove the effectiveness of the control loop, a similar experimental run  
 367 was started with an active control loop. The goal was to show that the controller is  
 368 able to automatically detect and react to the asymmetry as a result of interaction of  
 369 EMBr and the clogging model. The controller changes the set-point of EMBr current  
 370 to the predetermined value for which the hysteresis model was trained. The recording  
 371 of this experiment is shown in Figure 8. Once the experiment has started and the flow  
 372 is developed, the EMBr current is set to  $I_{EMBr} = 200$  A at  $t \approx 500$  s. A significant  
 373 asymmetry cannot be observed. After some time, we introduce the obstacle to the SEN  
 374 outlet. The obstacle does not have a fixed position, but rather, it is lowered until the  
 375 asymmetry occurs. At  $t \approx 620$  s a strong asymmetry becomes apparent. If the asymmetry  
 376 condition is satisfied for 15 s, the controller changes the set-point value to  $I_{EMBr} = 0$  A  
 377 at  $t \approx 700$  s. A significant reduction in asymmetry is noticeable, and we conclude that  
 378 the controller successfully executed the desired action. We repeated the test case starting  
 379 at  $t \approx 900$  s during the same measurement in order to validate the repeatability.

#### 380 4. Conclusions and outlook

381 The lab demonstration for the continuous casting model showed for the first time  
 382 that an electromagnetic actuator can be controlled based on the actual flow structure in  
 383 the mould. It is shown that CIFT can be used to monitor the flow in real-time even if

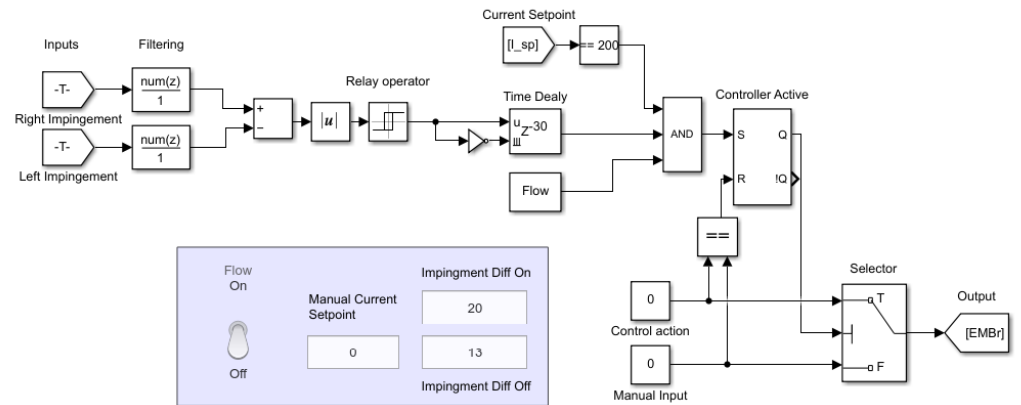


**Figure 7.** Real-Time SIMULINK implementation of the controller. The controller evaluates the difference of the jet impingement points on both sides. If the difference is within a window defined by the relay operator for 15 s, the controller will set a new EMBr current if the experiment is in operation, and EMBr current is at a valid set-point. Controller is reset and ready for new evaluation when the operator set a manual current set-point to be equal the controller value.

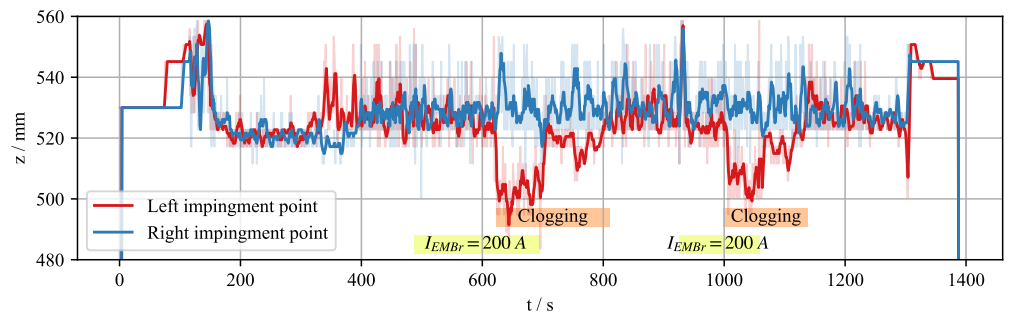


**Figure 8.** Controller validation experiment. The flow reaches a stable state by  $t = 200$  s. The same scenario is repeated twice during the same experiment. First, the EMBr current is set to  $I_{EMBr} = 200$  A at  $t \approx 500$  s and  $t \approx 900$  s.

384 the EMBr changes its strength, and it can be integrated into a control loop for an EMBr.  
385 The major challenge remains the accurate compensation of the effects of the change of  
386 EMBr current on CIFT. These effects are up to three orders of magnitude larger than the  
387 flow-induced signal.

388 As a first test case nozzle clogging was simulated by introducing an obstacle  
389 and partially blocking one of the outlet ports of the SEN, thus deflecting the flow.  
390 Under these circumstances, the impingement position of the jet moves downward when  
391 the EMBr is active. This undesired change of the jet impingement position can be  
392 corrected by switching off the EMBr. With this proof of concept, a working control loop  
393 implementation is available from now on, which is a valuable tool to investigate more  
394 sophisticated control strategies.

395 CIFT offers unique insights into the flow structure of the mould, and with that, a  
396 new way to monitor and control the process. The current controller implementation,  
397 albeit simple in nature, shows significant progress in using tomographic measurement  
398 techniques as a controller backbone. Further improvement of control strategies consists  
399 of increasing the measurement accuracy, robustness and speed, and identifying  
400 additional key flow features of interest for an efficient process. The next logical step  
401 is to implement a PI/PID controller and gradually increasing the complexity of the  
402 control algorithm, as one of the popular methods for tuning PID controllers is based on  
403 the relay control similar to what is shown in our experiments [41]. The PID controller  
404 could be used for controlling the impingement point of the jet in order to keep it in the  
405 certain range. This method of control could be then easily compared with the UDV  
406 measurements to quantify the accuracy and quality of compensation, reconstruction,  
407 and control.

408 Utilizing more complex control strategies will primarily require improving the  
409 compensation of the effects generated by the ferromagnetic parts. The two-way coupling  
410 of the reconstruction and compensation by the controller can result in unstable states  
411 and further precautions must be made to avoid them. This can be achieved by further  
412 enhancing the magnetization model or, perhaps, developing an additional inductive  
413 sensor, which detects the state of the magnetization vector in the yoke.

414 Future investigations should focus on generating a map of typical flow instabilities,  
415 which might be induced by higher liquid metal flow rates, Argon gas flow rates, nozzle  
416 clogging, bulging of the strand, etc. New control strategies can be achieved by using  
417 more sophisticated actuators, like local EMBr's, which independently influence the  
418 flow on both sides of the mould, or electromagnetic stirrers at the free surface. Such  
419 electromagnetic actuators are already available for continuous casters. Furthermore,  
420 new arrangements of the excitation coil and the magnetic field sensors for CIFT should  
421 be investigated. Last but not least, a more sophisticated solution of the inverse problem  
422 is pursued.

423 Further improvements might become possible by combining different tomography  
424 methods, so that key flow features could be mapped to flow instabilities and a controller  
425 could be upgraded. An example of this is the classification and identification of two-  
426 phase flows in the SEN using MIT. However, MIT system requires has to have high  
427 frame rate to capture the flow dynamic in the SEN. In any case, the main advantage of  
428 CIFT and MIT is that, because of their contactless nature, they can be implemented in  
429 aggressive industrial environment of steel casting, and provide information that was  
430 previously unavailable in order to improve the process control and design.

431 **Author Contributions:** Conceptualization, I.G. and T.W.; methodology, I.G.; software, I.G. and  
432 I.S.; validation, I.G. and T.W.; investigation, I.G.; resources, S.E. and T.W. ; data curation, I.G.;  
433 writing—original draft preparation, I.G., S.A., A.B., I.M.; writing—review and editing, T.W. and  
434 F.S.; visualization, I.G.; supervision, T.W., J.H., S.K., M.S.; All authors have read and agreed to the  
435 published version of the manuscript.

436 **Funding:** This research has received funding from the European Union's Horizon 2020 research  
437 and innovation programme under the Marie Skłodowska-Curie grant agreement No 764902

438 **Data Availability Statement:** Data supporting the reported results is available in open access.  
 439 [10.14278/rodare.1463](https://doi.org/10.14278/rodare.1463)

440 **Conflicts of Interest:** The authors declare no conflict of interest.

#### 441 Appendix A

442 In order to supply the data to the controller a real-time data evaluation pipeline has  
 443 been established, as depicted in block diagram in Figure A1. Main parts are real-time  
 444 demodulation, real-time compensation of the EMBr, real-time reconstruction, and the  
 445 controller itself. Initially, the induced voltage in the 14 coils is digitalized by the LTT24  
 446 A/D converter from the company Tasler, then filtered and subsequently demodulated  
 447 by a real-time demodulation procedure using the Lomb-Scargle method [36] at the  
 448 frequency of the excitation magnetic field. The resulting in-phase and out-phase voltages  
 449 are converted to the magnetic field with the transfer function of the gradiometric sensing  
 450 coils. The sampling frequency of the demodulated magnetic field is determined by the  
 451 number of periods used for demodulation. The in-phase and out-phase flow-induced  
 452 magnetic field is then sent to the compensation of the EMBr, which runs a real-time  
 453 discrete Krasnosel'skii-Pokrovski model of hysteresis, calculates the compensation value  
 454 based on the current and past values of the EMBr current, and the value is subtracted  
 455 from the demodulated in-phase and out-phase component of the flow-induced magnetic.  
 456 Velocity is reconstructed from the compensated in-phase flow-induced magnetic field  
 457 and the jet impingement positions are extracted, which are sent to the controller for  
 458 evaluation. Then, the controller decides on the set-point of the EMBr current.

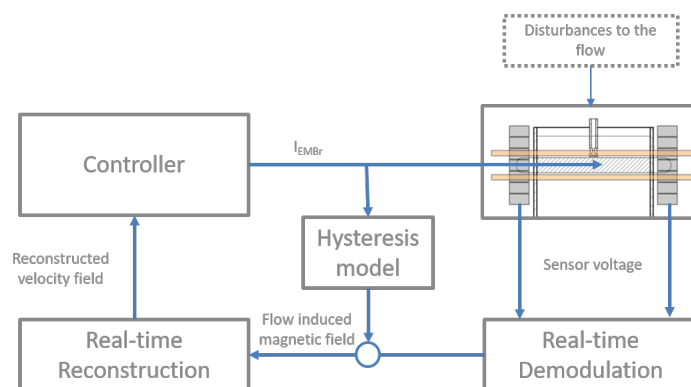
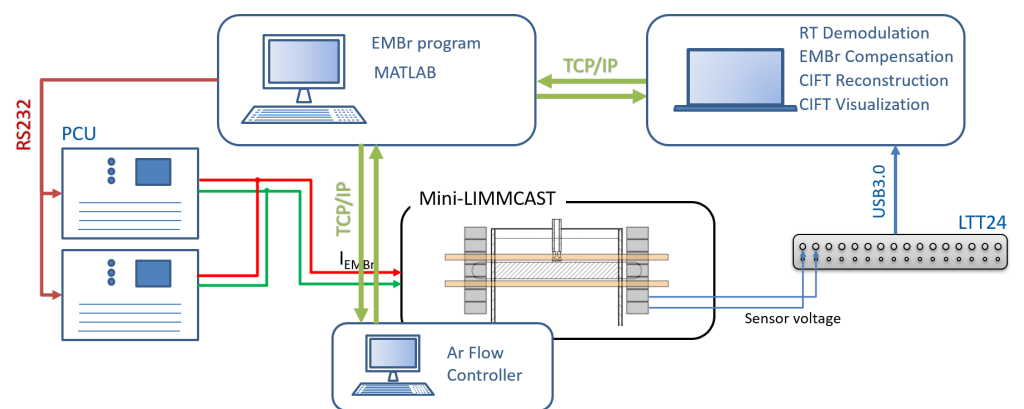


Figure A1. Block diagram showing the flow of information between the parts of the experiment

459 Figure A2 shows the network diagram of the experimental setup. Communication  
 460 interfaces between the individual programs used for reconstruction, demodulation,  
 461 visualisation and communication to the EMBr is done with TCP/IP sockets. This type of  
 462 connection allows for the ease of getting information from any step of the data processing  
 463 to another one. The hardware communication to the current sources for the EMBr is  
 464 realized via the serial RS232 port. The total time delay between the change in the flow  
 465 and final reconstruction is in the order of two seconds.





**Figure A2.** Communication network diagram showing the communication protocols between system parts

## References

1. Hibbeler, L.C.; Thomas, B.G. Mold Slag Entrainment Mechanisms in Continuous Casting Molds. In proceedings of the AISTech 2013.
2. Thomas, B.G.; Huang, X.; Sussman, R.C. Simulation of Argon Gas Flow Effects in a Continuous Slab Caster. *Metallurgical and Materials Transactions B* **1994**, *25*, 527–547.
3. Zhang, L.; Yang, S.; Cai, K.; Li, J.; Wan, X.; Thomas, B.G. Investigation of Fluid Flow and Steel Cleanliness in the Continuous Casting Strand. *Metallurgical and Materials Transactions B* **2007**, *38*, 63–83.
4. Cho, S.M.; Thomas, B.G. Electromagnetic Forces in Continuous Casting of Steel Slabs. *Metals* **2019**, *9*, 471.
5. Thomas, B.G.; Yuan, Q.; Sivaramakrishnan, S.; Shi, T.; Vanka, P.; Assar, M. B. Comparison of four methods to evaluate fluid velocities in a continuous casting mould. *Iron and Steel Institute of Japan International* **2001**, *41*, 1181–1193.
6. Liu, R.; Thomas, B.G.; Sengupta, J.; Chung, S.D.; Trinh, M. Measurements of Molten Steel Surface Velocity and Effect of Stopper-Rod Movement on Transient Multiphase Fluid Flow in Continuous Casting. *ISIJ International* **2014**, *10* 2314–23.
7. Dauby, P.H. Continuous casting: make better steel and more of it! *Revue de Métallurgie* **2012**, *109*, 113–136.
8. Zheng, J.; Runcong, L.; Wang, X.; Xu G.; LYU, Z.; Kolesnikov, Y.; Na, X.: An online contactless investigation of the meniscus velocity in a continuous casting mould using Lorentz Force Velocimetry, *Metallurgical and Materials Transactions B* **2020**, *41B*, 558–569.
9. Mul, M. Real-time Mould Temperature Control for the Purpose of Consistent Slab Quality. In proceedings of the METEC & 4th ESTAD, Düsseldorf 2019, Germany.
10. Hedin, G.; Kamperman, A.; Sedén, M.; Fröjdh, K.; Pejnefors, J. (2016). Exploring opportunities in mold temperature monitoring utilizing Fiber Bragg Gratings. In proceedings of the SCANMET V 2016, Luleå.
11. Zhang, T.; Yang, J.; Jiang, P. Measurement of Molten Steel Velocity near the Surface and Modeling for Transient Fluid Flow in the Continuous Casting Mold. *Metals* **2019**, *9*, 36.
12. Hashimoto, Y.; Matsui, A.; Hayase, T.; Kano, M. Real-time estimation of molten steel flow in continuous casting mold. *Metallurgical and Materials Transactions B* **2020**, *51*, 581–588.
13. Cukierski, Kevin; Thomas, B. G. Flow Control with Local Electromagnetic Braking in Continuous Casting of Steel Slabs. *Metallurgical and Materials Transactions B* **2008**, *39*, 94–107.
14. Okazawa, K.; Toh, T.; Fukuda, J.; Kawase, T.; Toki, M. Fluid Flow in a Continuous Casting Mold Driven by Linear Induction Motors. *ISIJ International* **41** bf 2001, *8*, 851–58.
15. Schurmann, D.; Glavinić, I.; Willers, B.; Timmel, K.; Eckert, S. Impact of the Electromagnetic Brake Position on the Flow Structure in a Slab Continuous Casting Mold: An Experimental Parameter Study. *Metallurgical and Materials Transactions B* **2019**, *51*, 61–78.
16. Jin, X.; Chen, F. D.; Zhang, J.; Xie, X.; Bi, Y. Y. 2011. Water Model Study on Fluid Flow in Slab Continuous Casting Mould with Solidified Shell. *Ironmaking & Steelmaking* **38** **2011**, *38*, 155–159.
17. Ramirez L. P.; Bjorkvall, J.; Olofsson, C.; Nazem J. P.; Sjoström, U.; Nilsson, C. Continuous Casting Simulator for Measurement and Control of Liquid Metal Flow in the Mould. In proceedings of the 8th European Continuous Casting Conference 2014, Austria.
18. Timmel, K.; Eckert, S.; Gerbeth, G.; Stefani, F.; Wondrak, T. Experimental Modeling of the Continuous Casting Process of Steel Using Low Melting Point Metal Alloys - the LIMMCAST Program. *ISIJ International* **2010**, *50*, 1134–1141.
19. Dekemele, K.; Ionescu, C.; De Doncker, M.; De Keyser, R. Closed loop control of an electromagnetic stirrer in the continuous casting process. In proceedings of the 2016 European Control Conference 2016, 61–66.
20. Watzinger, J.; Watzinger, I. Latest advancements in ESP casting technology, In proceedings of the European Continuous Casting Conference 2021.
21. Ma, X.; Peyton, A.J.; Higson, S.R.; Lyons, A.; Dickinson, S.J. Hardware and software design for an electromagnetic induction tomography (EMT) system for high contrast metal process applications. *Measurement Science and Technology* **2006**, *17*, 111.
22. Stefani, F.; Gerbeth, G. A contactless method for velocity reconstruction in electrically conducting fluids. *Measurement Science and Technology* **2000**, *11*, 758–765.
23. Terzija, N.; Yin, W.; Gerbeth, G.; Stefani, F.; Timmel, K.; Wondrak, T.; Peyton, A. Electromagnetic inspection of a two-phase flow of GaInSn and Argon. *Flow Measurement and Instrumentation* **2011**, *22*, 10–16.
24. Wondrak, T.; Eckert, S.; Gerbeth, G.; Klotsche, K.; Stefani, F.; Timmel, K.; Peyton, A. J.; Terzija, N.; Yin, W. Combined electromagnetic tomography for determining two-phase flow characteristics in the submerged entry nozzle and in the mold of a continuous casting model. *Metallurgical and Materials Transactions B* **2011**, *42*, 1201–1210.
25. Muttakin, I.; Soleimani, M. Interior void classification in liquid metal using multi-frequency magnetic induction tomography with a machine learning approach. *IEEE Sensors Journal* **2021**, *21*, 23289–23296.
26. Stefani, F.; Gundrum, T.; Gerbeth, G. Contactless Inductive Flow Tomography. *Physical Review E* **70** **2004**, *5*, 056306.
27. Wondrak, T.; Galindo, V.; Gerbeth, G.; Gundrum, T.; Stefani, F.; Timmel, K. Contactless inductive flow tomography for a model of continuous steel casting. *Measurement Science and Technology* **2010**, *21*, 045402.
28. Wondrak, T.; Pal, J.; Stefani, F.; Galindo, V.; Eckert, S. Visualization of the global flow structure in a modified Rayleigh-Bénard setup using contactless inductive flow tomography. *Flow Measurement and Instrumentation* **2018**, *61*, 269–280.
29. Ratajczak, M.; Wondrak, T.; Stefani, F. A gradiometric version of contactless inductive flow tomography: theory and first applications. *Philosophical Transactions A* **2016**, *374*, 20150330.

30. Ratajczak, M.; Wondrak, T. Analysis, design and optimization of compact ultra-high sensitivity coreless induction coil sensors. *Measurement Science and Technology* **2020**, *31*, 065902.
31. Ratajczak, M.; Wondrak, T.; Timmel, K.; Stefani, F.; Eckert, S. Flow Visualization by Means of Contactless Inductive Flow Tomography in the Presence of a Magnetic Brake. *Journal for Manufacturing Science and Production* **2015**, *15*, 41–48.
32. Ratajczak, M.; Wondrak, T.; Stefani, F.; Eckert, S. Numerical and experimental investigation of the contactless inductive flow tomography in the presence of strong static magnetic fields. *Magnetohydrodynamics* **2015**, *51*, 461–471.
33. Glavinić, I.; Stefani, F.; Eckert, S.; Wondrak, T. Real time flow control during continuous casting with contactless inductive flow tomography. In proceedings of the 10th International Conference on Electromagnetic Processing of Materials 2021, 14-16 June 2021, 170–175.
34. Wondrak, T.; Jacobs, R. T.; Faber, P. Fast Reconstruction Algorithm for Contactless Inductive Flow Tomography. In proceedings of the 10th International Conference on Advanced Computer Information Technologies 2020, 217–20.
35. Abouelazayem, S.; Glavinić, I.; Wondrak, T.; Hlava, J. Flow Control Based on Feature Extraction in Continuous Casting Process. *Sensors* **2020**, *20*, 6880.
36. Lomb, N.R., Least-square frequency analysis of unequally spaced data. *Astrophysics and Space Science* **1976**, *39*, 447–462.
37. Mayergoyz, I. D. Mathematical Models of Hysteresis. *Physical Review Letters* **56** **1986**, 1518–21.
38. Krasnosel'skiĭ, M. A., Pokrovskiĭ, A. V. *Systems with Hysteresis*. Heidelberg: Springer Berlin Heidelberg, Berlin, 1989.
39. Stakvik, J. Å.; Ragazzon, R.P. M.; Eielsen, A. A.; Gravdahl, J. T. On Implementation of the Preisach Model: Identification and Inversion for Hysteresis Compensation. *Modeling, Identification and Control: A Norwegian Research Bulletin* **36** **2015**, *3*, 133–42.
40. Cho, S.M; Kim, S. H.; Chaudhary, R.; Thomas, B.G.; Shin, H. J.; Choi, W. R.; Kim, S.K. Effect of Nozzle Clogging on Surface Flow and Vortex Formation in the Continuous Casting Mold. In proceedings of the AISTech 2011, Indianapolis, Indiana, USA.
41. Hang, C. C.; Astrom, K. J.; Wang, Q. G. Relay Feedback Auto-Tuning of Process Controllers — a Tutorial Review. *Journal of Process Control* **12** **2002**, *1*, 143–62.